

Local finite element enrichment strategies for 2D contact computations and a corresponding post-processing scheme

Roger A. Sauer ¹

Aachen Institute for Advanced Study in Computational Engineering Science (AICES), RWTH Aachen University, Templergraben 55, 52056 Aachen, Germany

Published² in *Computational Mechanics*, DOI: [10.1007/s00466-012-0813-8](https://doi.org/10.1007/s00466-012-0813-8)
Submitted on 21 March, Revised on 7 September 2012, Accepted on 18 October 2012

Abstract

Recently an enriched contact finite element formulation has been developed that substantially increases the accuracy of contact computations while keeping the additional numerical effort at a minimum (Sauer, 2011). Two enrichment strategies were proposed, one based on local p-refinement using Lagrange interpolation and one based on Hermite interpolation that produces C^1 -smoothness on the contact surface. Both classes, which were initially considered for the frictionless Signorini problem, are extended here to friction and contact between deformable bodies. For this, a symmetric contact formulation is used that allows the unbiased treatment of both contact partners. This paper also proposes a post-processing scheme for contact quantities like the contact pressure. The scheme, which provides a more accurate representation than the raw data, is based on an averaging procedure that is inspired by mortar formulations. The properties of the enrichment strategies and the corresponding post-processing scheme are illustrated by several numerical examples considering sliding and peeling contact in the presence of large deformations.

Keywords: cohesive zone modeling, computational contact mechanics, enhanced finite elements, nonlinear finite element methods, peeling, sliding friction

1 Introduction

It is well known that coarse finite element discretizations can lead to oscillatory load-displacement curves for sliding (Laursen, 2002; Wriggers, 2006) and peeling contact (Crisfield and Alfano, 2002). In the past, various contact smoothing techniques have been proposed to address this issue, e.g. see El-Abbasi et al. (2001); Padmanabhan and Laursen (2001); Wriggers et al. (2001). These techniques consider the smoothing of the master surface in order to increase the accuracy of the evaluation of the contact forces. Beyond that, it is also useful to smoothen the slave surface in order to increase the accuracy of the contact integrals. This can be achieved by high-order FE interpolation based on Lagrange (Puso et al., 2008), hierarchic (Franke et al., 2010) or NURBS interpolation (Temizer et al., 2011; De Lorenzis et al., 2011). These approaches use high-order interpolation throughout the discretized domain. As an alternative, one can also consider just using high-order interpolation on the contact surface, and resorting to standard linear interpolation within the domain.

Such a local contact enrichment strategy was proposed in Sauer (2011), and it was shown there

¹Email: sauer@aices.rwth-aachen.de

²This pdf is the personal version of an article whose final publication is available at www.springerlink.com

that the approach increases accuracy and robustness for contact computations, while keeping the additional numerical effort at a minimum. The enrichment strategy is based on high-order Lagrange and Hermite interpolation. The latter provides a discretization that is C^1 -continuous on the contact surface but remains C^0 elsewhere. Such a setup seems ideal for contact computations that are typically governed by the accuracy of the contact contributions. Consequently, large accuracy gains are achieved for the sliding and peeling examples of [Sauer \(2011\)](#). These examples are restricted to Signorini contact conditions. It remains to be shown that local enrichment strategies also achieve accuracy and robustness gains for friction and contact between deformable contact partners. This is the purpose of the present paper.

A further objective of this paper is to present a novel post-processing scheme for contact quantities like the contact pressure. Such a scheme is useful, since the pressures obtained through other means can be oscillatory and inaccurate.

The remainder of this paper is structured as follows. [Sec. 2](#) presents the theory of the contact models considered here. [Sec. 3](#) reviews the enriched contact FE formulation of [Sauer \(2011\)](#) and presents the novel contact post-processing scheme ([Sec. 3.4](#)). Numerical examples are then shown in [Sec. 4](#). The paper concludes with [Sec. 5](#).

2 Considered contact models

This section discusses the continuum mechanical equations for contact, considering classical penalty formulations, Coulomb friction and cohesive zone models.

Consider two bodies, denoted \mathcal{B}_1 and \mathcal{B}_2 ,³ that can come into contact and undergo large deformations. For a quasi-static contact problem, the deformation field $\varphi = \{\varphi_1, \varphi_2\}$ of \mathcal{B}_1 and \mathcal{B}_2 satisfies the weak form

$$\delta\Pi(\varphi, \delta\varphi) = \delta\Pi_{\text{int}} + \delta\Pi_{\text{c}} - \delta\Pi_{\text{ext}} = 0, \quad \forall \delta\varphi \in \mathcal{V}, \quad (1)$$

where $\delta\Pi_{\text{int}}$ and $\delta\Pi_{\text{ext}}$ denote the internal and external virtual work contributions and \mathcal{V} is a suitable function space for the virtual displacement field $\delta\varphi$. Further, $\delta\Pi_{\text{c}} = \delta\Pi_{\text{c}1} + \delta\Pi_{\text{c}2}$ denotes the virtual work of the contact forces. For each body \mathcal{B}_k ($k = 1, 2$), the virtual contact work can be written as

$$\delta\Pi_{\text{c}k} = - \int_{\partial_{\text{c}}\mathcal{B}_k} \mathbf{t}_k \cdot \delta\varphi_k \, da_k, \quad (2)$$

i.e. the contact tractions \mathbf{t}_1 and \mathbf{t}_2 are each integrated over the current contact surface $\partial_{\text{c}}\mathcal{B}_k$ where they act on.⁴ Here, $da_k \subset \partial_{\text{c}}\mathcal{B}_k$ denotes a surface element in the current configuration. A formulation of this kind was initially proposed by [Papadopoulos et al. \(1995\)](#). Expression (2) can be derived from a global contact potential Π_{c} ([Sauer and De Lorenzis, 2012](#)). It leads to a robust and efficient contact algorithm that is unbiased w.r.t. the two contact surfaces ([Sauer and De Lorenzis, 2012](#)). This algorithm is discussed further in [Sec. 3](#). Introducing the scaled traction

$$\mathbf{T}_k := \lambda_k^{\text{s}} \mathbf{t}_k, \quad (3)$$

where

$$\lambda_k^{\text{s}} := \frac{\partial a_k}{\partial A_k} \quad (4)$$

³The symbols \mathcal{B}_1 and \mathcal{B}_2 are also used to denote the current configuration of the bodies.

⁴ k is just the index for body \mathcal{B}_k ; no summation over k is implied here or elsewhere.

denotes the surface stretch between the current area element $da_k \subset \partial\mathcal{B}_k$ and the corresponding reference area element $dA_k \subset \partial\mathcal{B}_{0k}$, eq. (2) can be rewritten into the equivalent expression

$$\delta\Pi_{ck} = - \int_{\partial_c\mathcal{B}_{0k}} \mathbf{T}_k \cdot \delta\boldsymbol{\varphi}_k dA_k , \quad (5)$$

which is now integrated over the contact surface in the reference configuration.

2.1 Normal contact formulation

We consider here the classical penalty method for normal contact, given by⁵

$$\mathbf{t}_k = \begin{cases} -\epsilon_n g_n \mathbf{n}_p & \text{for } g_n < 0 , \\ 0 & \text{for } g_n \geq 0 , \end{cases} \quad (6)$$

where ϵ_n is the penalty parameter. The length g_n denotes the normal gap between the two bodies, see Fig. 1. For a given surface point $\mathbf{x}_k \in \partial\mathcal{B}_k$, the gap is defined by

$$g_n := (\mathbf{x}_k - \mathbf{x}_p) \cdot \mathbf{n}_p , \quad (7)$$

where $\mathbf{x}_p \in \partial\mathcal{B}_\ell$ denotes the closest projection point of \mathbf{x}_k on the neighboring body \mathcal{B}_ℓ ($\ell \neq k$). \mathbf{x}_p is specified by the convective coordinate ξ that describes the surface points $\mathbf{x}_\ell(\xi) \in \partial\mathcal{B}_\ell$. Denoting ξ_p as the coordinate of \mathbf{x}_p we thus have

$$\mathbf{x}_p = \mathbf{x}_\ell|_{\xi=\xi_p} . \quad (8)$$

The unit vector \mathbf{n}_p denotes the surface normal of $\partial\mathcal{B}_\ell$ at projection point $\mathbf{x}_p \in \partial\mathcal{B}_\ell$. For a discrete surface that is only C^0 -continuous, the surface normal jumps at the finite element nodes. Therefore, it is practical to define the normal as

$$\mathbf{n}_p := \frac{\mathbf{x}_k - \mathbf{x}_p}{g_n} \quad (9)$$

and evaluate the gap from

$$g_n = \pm \sqrt{(\mathbf{x}_k - \mathbf{x}_p) \cdot (\mathbf{x}_k - \mathbf{x}_p)} . \quad (10)$$

An alternative is to average \mathbf{n}_p at the element nodes (Yang et al., 2005). This is not considered here.

2.2 Frictional contact formulation

For the description of frictional contact, the contact traction is decomposed into normal and tangential components, i.e.

$$\mathbf{t}_k = p_k \mathbf{n}_p + \tau_k \bar{\mathbf{a}}_p , \quad (11)$$

where $p_k = \mathbf{t}_k \cdot \mathbf{n}_p$ denotes the contact pressure and $\tau_k = \mathbf{t}_k \cdot \bar{\mathbf{a}}_p$ denotes the contact shear traction. Here, the former is taken from eq. (6). The unit vector $\bar{\mathbf{a}}_p$ denotes the normalized tangent vector of $\partial\mathcal{B}_\ell$ at \mathbf{x}_p . It is obtained from the normalization of the tangent vector

$$\mathbf{a}_p = \frac{\partial \mathbf{x}_p}{\partial \xi_p} , \quad (12)$$

⁵Note, that this formulation misses an additional, negligible term to be variationally consistent (Fischer and Wriggers, 2005; Sauer and De Lorenzis, 2012).

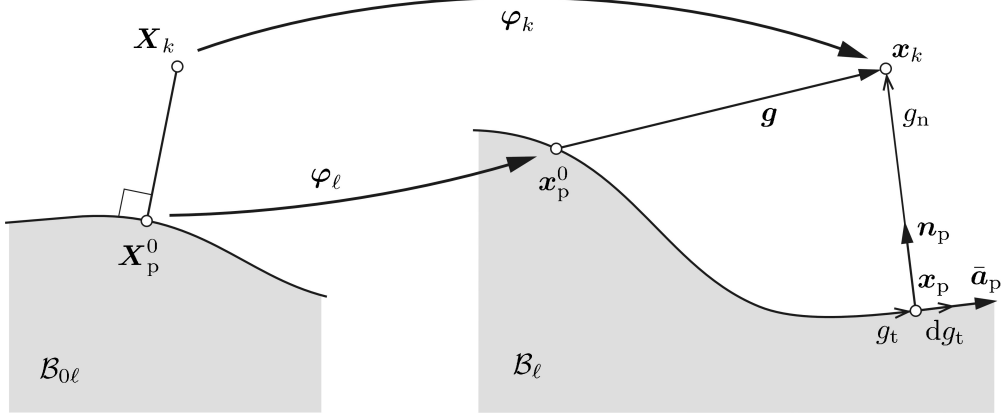


Figure 1: Definition of the kinematic contact quantities \mathbf{g} , g_n and g_t for a given point \mathbf{x}_k and surface $\partial\mathcal{B}_\ell$.

i.e. $\bar{\mathbf{a}}_p = \mathbf{a}_p / \hat{a}_p$ for $\hat{a}_p := \sqrt{\mathbf{a}_p \cdot \mathbf{a}_p}$.

In frictional contact two mechanisms are distinguished: Sticking friction and sliding friction. The distinction is based on the slip criterion

$$f_s \begin{cases} < 0 & \text{sticking ,} \\ = 0 & \text{sliding ,} \end{cases} \quad (13)$$

where

$$f_s = |\tau_k| - \mu p_k . \quad (14)$$

$f_s = 0$ denotes a surface in traction state space $\mathbf{t}_k = \{p_k, \tau_k\}$. During sliding the contact traction is constrained to stay on this surface. For the description of sticking we consider the penalty method.

The shear traction τ_k is related to g_t , which denotes the sliding path of the projection point \mathbf{x}_p on surface $\partial\mathcal{B}_\ell$ as shown in Fig. 1. Here,

$$\mathbf{x}_p^0 := \varphi_\ell(\mathbf{X}_p^0) \quad (15)$$

denotes the current position of the initial projection point $\mathbf{X}_p(t_0)$. The sliding path is found from integrating the slip increment (Wriggers, 2006)

$$dg_t = \hat{a}_p d\xi_p . \quad (16)$$

The tangential slip is decomposed into two parts, a reversible (elastic) part, g_e , that is recovered upon unloading and is associated with sticking, and an irreversible (inelastic) part, g_s , that is not recovered upon unloading and is associated with sliding, i.e.

$$g_t = g_e + g_s . \quad (17)$$

To assess the decomposition, an evolution law for the inelastic slip is required. The change in g_s points in the direction of τ_k , i.e. we have

$$\dot{g}_s = \gamma \frac{\tau_k}{|\tau_k|} , \quad (18)$$

where the parameter $\gamma = |\dot{g}_s| > 0$ describes the proportionality. Evolution law (18) needs to be integrated in time. Therefore, we consider a discretization in time, and march from time step

t_n to t_{n+1} .⁶ In this manner we find the new slip

$$g_t^{n+1} = g_t^n + \Delta g_t^{n+1} , \quad (19)$$

with

$$\Delta g_t^{n+1} = \hat{a}_p^{n+1} (\xi_p^{n+1} - \xi_p^n) \quad (20)$$

according to eq. (16) and the implicit Euler integration scheme. To simplify the notation, index $n + 1$ is omitted in the following. All quantities without this index are now understood to be evaluated at t_{n+1} . Given the slip contributions g_t^n and g_s^n at t_n and the new slip g_t at t_{n+1} we can now find the new inelastic slip at t_{n+1} by applying implicit Euler to eq. (18), i.e.

$$g_s = g_s^n + \Delta \gamma \frac{\tau_k}{|\tau_k|} . \quad (21)$$

In order to obtain the shear τ_k at t_{n+1} , a predictor-corrector algorithm is used. At t_{n+1} , the additional slip Δg_t is first predicted to be an additional elastic slip, i.e. $\Delta g_t = \Delta g_e$ and $\Delta g_s = 0$. According to the penalty method the traction τ_k is assumed to be proportional to g_e . We thus find

$$\tau_k^{\text{trial}} = -\epsilon_t (g_t - g_s^n) , \quad (22)$$

where the superscript ‘trial’ refers to the fact that this is only a prediction. With this prediction the slip criterion (14) is checked. If a violation is detected (i.e. if $f_s(\tau_k^{\text{trial}}) > 0$), sliding occurs and the traction needs to be corrected. According to Coulomb’s sliding law, we now have

$$\tau_k = \mu p_k \frac{\dot{g}_s}{|\dot{g}_s|} , \quad (23)$$

which follows directly from $f_s = 0$ and eq. (18). It can be further shown that

$$\frac{\dot{g}_s}{|\dot{g}_s|} = \frac{\tau_k}{|\tau_k|} = \frac{\tau_k^{\text{trial}}}{|\tau_k^{\text{trial}}|} = \text{sign } \tau_k^{\text{trial}} =: \bar{\tau}_k^{\text{trial}} . \quad (24)$$

If sliding occurs, we need to compute the new inelastic slip g_s from eq. (21). Enforcing $f_s(\tau_k) = 0$, we find

$$\Delta \gamma = \frac{f_s(\tau_k^{\text{trial}})}{\epsilon_t} . \quad (25)$$

If no additional sliding occurs we have $\Delta \gamma = 0$.

2.3 Cohesive zone formulation

This formulation considers cohesion between the surface points $\mathbf{x}_k \in \partial \mathcal{B}_k$ and $\mathbf{x}_p^0 \in \partial \mathcal{B}_\ell$, where \mathbf{x}_p^0 denotes the current location of the original projection point \mathbf{X}_p^0 obtained at t_0 , see Fig. 1. The gap and the direction between \mathbf{x}_k and \mathbf{x}_p^0 are obtained from

$$g = \|\mathbf{g}\| , \quad \mathbf{g} := \mathbf{x}_k - \mathbf{x}_p^0 , \quad \bar{\mathbf{g}} := \frac{\mathbf{g}}{g} . \quad (26)$$

Cohesion is considered to occur at a fixed number of bonds per surface area. This bond density is denoted by β_k^s . Each bond produces the force \mathbf{F}_k upon separation, such that the traction becomes $\mathbf{t}_k = \beta_k^s \mathbf{F}_k$. The number of bonds is considered to remain invariant under deformation, i.e.

$$\beta_k^s da_k = \beta_{0k}^s dA_k = \text{const.} , \quad (27)$$

⁶The variable t does not need to describe actual time. It can also be associated to the computational load stepping.

where β_{0k}^s denotes the number of bonds per reference surface area. It is therefore convenient to formulate cohesion w.r.t. the undeformed (reference) surface, i.e. in terms of the surface traction $\mathbf{T}_k = \beta_{0k}^s \mathbf{F}_k$. Here we consider the separation model

$$\mathbf{T}_k = -T_0 \frac{g}{g_0} \exp\left(1 - \frac{g}{g_0}\right) \bar{\mathbf{g}}, \quad (28)$$

where T_0 and g_0 are model constants. This model is a special case of the classical cohesive zone model of [Xu and Needleman \(1993\)](#). Note, that this model considers equal energy in mode I and mode II debonding. This model combines normal and tangential (sticking) contact. Cohesive zone model (28) can be extended to damage. This is not considered here.

3 Enriched contact finite elements

3.1 Enrichment formulation

First, we briefly describe the enrichment formulation of [Sauer \(2011\)](#). This formulation provides a high-order contact representation while using a low-order representation in the domain. In contrast to standard interpolation, this allows a much more accurate integration of the surface integrals, which is very beneficial for contact. The enrichment is based on local, high-order Lagrange and Hermite interpolation. The elements that are constructed in this way are shown in Fig. 2. Here Q1C1 denotes the standard quadrilateral element, which uses linear interpolation

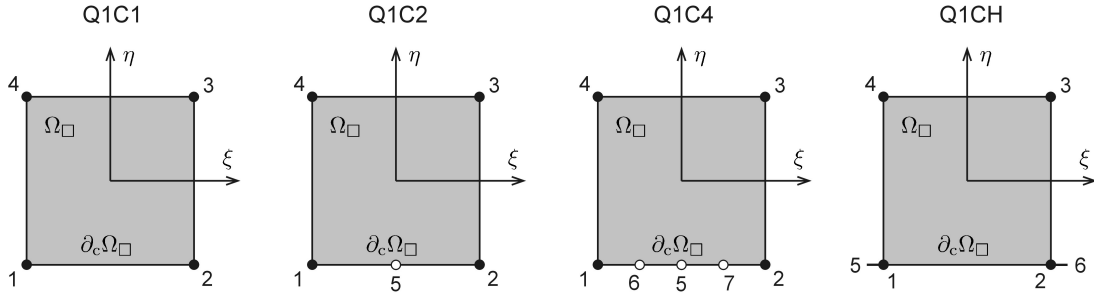


Figure 2: Enriched contact finite elements: standard linear element (Q1C1); quadratic enrichment (Q1C2); quartic enrichment (Q1C4); Hermite enrichment (Q1CH). The figure shows the master domain Ω_\square with contact surface $\partial_c \Omega_\square$, which is then mapped to the undeformed and deformed element domains Ω_{0k}^e and Ω_k^e with contact surfaces Γ_{0k}^e and Γ_k^e .

both in the domain and on the contact surface. Q1C2 and Q1C4 denote Lagrange-enriched contact elements that use quadratic and quartic Lagrange interpolation on the contact surface, while the interpolation is linear otherwise. Q1CH denotes the Hermite-enriched contact element, which provides a C^1 -continuous surface representation while the domain remains C^0 -continuous.

In all cases the displacement field within element Ω_k^e is interpolated by the approximation

$$\mathbf{u}_k(\boldsymbol{\xi}) \approx \mathbf{N}_k(\boldsymbol{\xi}) \mathbf{u}_k^e, \quad \boldsymbol{\xi} \in \Omega_\square. \quad (29)$$

A likewise interpolation is used for the deformation field \mathbf{x}_k , the reference configuration \mathbf{X}_k and the virtual displacement field $\delta\boldsymbol{\varphi}_k$. In eq. (29),

$$\mathbf{N}_k = [N_1 \mathbf{I}, N_2 \mathbf{I}, \dots, N_{n_k^e} \mathbf{I}] \quad (30)$$

is an array with size $n_{\text{dim}} \times n_{\text{dim}} n_k^e$, where, in 2D, $n_{\text{dim}} = 2$ and $n_k^e = 4$ for Q1C1, $n_k^e = 5$ for Q1C2, $n_k^e = 7$ for Q1C4 and $n_k^e = 6$ for Q1CH. $N_I = N_I(\boldsymbol{\xi})$, for $I = 1, \dots, n_k^e$, denote the shape functions of element Ω_k^e , which are given in [Sauer \(2011\)](#) for the four different element classes of Fig. 2. In case of Hermite interpolation, N_5 and N_6 denote the shape functions of the derivative-degrees-of-freedom. On the contact surface, Γ_k^e , interpolation (29) can be reduced to the surface nodes, i.e. we then have $n_k^e = 2$ for Q1C1, $n_k^e = 3$ for Q1C2, $n_k^e = 5$ for Q1C4 and $n_k^e = 4$ for Q1CH.

Interpolation (29) satisfies the partition of unity, where each N_I has a compact support. The support radius is just one element ([Sauer, 2011](#)). Note that for NURBS surface representations the support radius tends to be much larger.

3.2 Discretized weak form

Discretized, eq. (1) takes the form

$$\mathbf{v}^T [\mathbf{f}_{\text{int}} + \mathbf{f}_{\text{c}} - \mathbf{f}_{\text{ext}}] = 0, \quad \forall \mathbf{v} \in \mathcal{V}^h. \quad (31)$$

where \mathcal{V}^h is a suitable space for the virtual nodal displacements \mathbf{v} . Here \mathbf{f}_{int} , \mathbf{f}_{c} and \mathbf{f}_{ext} denote the nodal forces corresponding to the virtual work contributions $\delta\Pi_{\text{int}}$, $\delta\Pi_{\text{c}}$ and $\delta\Pi_{\text{ext}}$. From the discretized weak form (31) we can extract the equation

$$\mathbf{f}(\mathbf{u}) = \mathbf{f}_{\text{int}} + \mathbf{f}_{\text{c}} - \mathbf{f}_{\text{ext}} = \mathbf{0}, \quad (32)$$

which describes force equilibrium at the free finite element nodes. The forces \mathbf{f}_{int} , \mathbf{f}_{c} and \mathbf{f}_{ext} are assembled from the elemental contributions $\mathbf{f}_{\text{int}k}^e$, $\mathbf{f}_{\text{c}k}^e$ and $\mathbf{f}_{\text{ext}k}^e$ obtained from the integration over the volume elements Ω_k^e and surface elements Γ_k^e . $\mathbf{f}_{\text{int}k}^e$ is computed from the internal stress field; see ([Wriggers, 2008](#)) for details. In the following examples we consider the Neo-Hookean material model

$$\boldsymbol{\sigma} = \frac{\Lambda}{J} (\ln J) \mathbf{I} + \frac{\mu}{J} (\mathbf{F}\mathbf{F}^T - \mathbf{I}), \quad (33)$$

where J is the determinant of the deformation gradient $\mathbf{F} = \text{Grad } \boldsymbol{\varphi}$. Λ and μ correspond to the bulk and shear moduli (in the linear elastic regime). They are related to Young's modulus E and Poisson's ratio ν , via $\Lambda = 2\mu\nu/(1-2\nu)$ and $\mu = E/2/(1+\nu)$. For the following examples, we further consider $\mathbf{f}_{\text{ext}} = \mathbf{0}$. $\mathbf{f}_{\text{c}k}^e$ is discussed below.

3.3 Contact formulation

The contact force vector on surface element $\Gamma_k^e \subset \partial\mathcal{B}_k^h$ is given by

$$\mathbf{f}_{\text{c}k}^e = - \int_{\Gamma_{0k}^e} \mathbf{N}_k^T \mathbf{T}_k \, dA_k = - \int_{\Gamma_k^e} \mathbf{N}_k^T \mathbf{t}_k \, da_k, \quad (34)$$

which follows readily from eqs. (2) and (5). Numerical quadrature is considered to integrate (34). The contact traction \mathbf{t}_k (\mathbf{T}_k respectively) is then evaluated at every quadrature point using eq. (6) for frictionless contact, eq. (11) for frictional contact and eq. (28) for cohesive separation. All contact quantities are evaluated w.r.t the current configuration of the two bodies. Expression (34) is evaluated equivalently for both surfaces ($k = 1, 2$). This approach, named *the two-half-pass contact algorithm* is discussed in detail in [Sauer and De Lorenzis \(2012\)](#). It is unbiased w.r.t. the contact surface and is more robust and efficient than classical one-pass contact algorithms. [Sauer and De Lorenzis \(2012\)](#) also contains the tangent matrices

for expression (34). If one body is considered rigid, formulation (34) is equal to the one-pass approach of Fischer and Wriggers (2005).

For large penalty parameters and a high number of quadrature points, formulation (34) can converge poorly. The example in Sec. 4.3 shows that this problem is remedied by the contact enrichment proposed here. Alternatively one can also consider a Mortar description. This will be considered in future research.

Next, we discuss the computation of \mathbf{x}_p , \mathbf{a}_p and λ_k^s for a surface discretization based on the elements shown in Fig. 2. The projection point is given by

$$\mathbf{x}_p = \sum_I N_I(\xi_p) \mathbf{x}_I^\ell, \quad (35)$$

where $\mathbf{x}_I^\ell \in \partial\mathcal{B}_\ell^h$ denote the positions of the surface nodes. The tangent vector then follows as

$$\mathbf{a}_p = \frac{\partial \mathbf{x}_p}{\partial \xi} = \sum_I N_{I,\xi}(\xi_p) \mathbf{x}_I^\ell, \quad (36)$$

where $N_{I,\xi} := \partial N_I / \partial \xi$. The coordinate of the projection point, ξ_p , is found from solving the nonlinear equation

$$f = (\mathbf{x}_p - \mathbf{x}_k) \cdot \mathbf{a}_p = 0. \quad (37)$$

See Wriggers (2006) or Sauer and De Lorenzis (2012) for details. In 2D, the surface stretch describes the change of lengths from the reference to the current configuration and can thus be obtained from

$$\lambda_k^s = \frac{\|\mathbf{a}_k\|}{\|\mathbf{A}_k\|} = \frac{\sqrt{\mathbf{a}_k \cdot \mathbf{a}_k}}{\sqrt{\mathbf{A}_k \cdot \mathbf{A}_k}} = \frac{\hat{a}_k}{\hat{A}_k}, \quad (38)$$

with $\hat{a}_k := \sqrt{\mathbf{a}_k \cdot \mathbf{a}_k}$ and $\hat{A}_k := \sqrt{\mathbf{A}_k \cdot \mathbf{A}_k}$. In analogy to (36),

$$\begin{aligned} \mathbf{a}_k &= \frac{\partial \mathbf{x}_k}{\partial \xi} = \sum_I N_{I,\xi} \mathbf{x}_I^k, \\ \mathbf{A}_k &= \frac{\partial \mathbf{X}_k}{\partial \xi} = \sum_I N_{I,\xi} \mathbf{X}_I^k \end{aligned} \quad (39)$$

denote the tangent vectors at $\mathbf{x}_k \in \partial\mathcal{B}_k^h$ and $\mathbf{X}_k \in \partial\mathcal{B}_{0k}^h$.

The tangent matrices associated with the above contact formulation are discussed in Sec. A. Due to the compact support of the enrichment formulation, the coupling terms only involve single element pairs from the two neighboring surfaces. This keeps the complexity and the matrix fill-in minimal.

3.4 A post-processing scheme for the contact pressure

In order to compare the performance of the different contact element formulations it is useful to examine the contact pressure. Here the question arises which pressure to consider. One can for example extract the contact pressure from the FE stress field $\boldsymbol{\sigma}$, or one can extract it from the FE contact traction \mathbf{t} , defined here continuously along the surface according to the models of Sec. 2. But both these choices have deficiencies: The stress field is not very accurate for displacement based finite elements, since it is related to the derivative of the displacements. The surface traction, on the other hand, can be highly oscillatory, especially for the penalty method with large penalty parameters (Sauer, 2011; Temizer et al., 2011; De Lorenzis et al., 2011). The

problem can be seen from the following example: Consider using linear finite elements to model contact with a curved surface such that $g_n \geq 0$. Further consider using contact formulation (34) and (6) with infinitely many quadrature points. In this case the contact constraint $g_n = 0$ can only be satisfied at one quadrature point, while for all other points one must have $g_n > 0$. In theory we thus obtain a singular pressure at this point while the pressure is zero elsewhere. Above that, the contact traction is in itself not an equilibrated quantity, since equilibrium is only satisfied at the finite element nodes.

This motivates the construction of a post-processed pressure field that is both smoother and more accurate than raw pressure data. We therefore propose an averaging scheme for the pressure field that is inspired by the mortar formulation used in Temizer et al. (2011).

In general, the averaging is constructed as follows. Consider a field quantity $f_k(s)$ defined on the contact surface $\partial_c \mathcal{B}_k$.⁷ Here, the variable s is used to denote the coordinate along the current surface. An example is the contact pressure $p_k(s)$. We now seek an accurate approximation to $f_k(s)$ that is free from the deficiencies noted above. It is natural to use the FE interpolation for this, i.e. we construct a post-processed field $f_k^{\text{P}}(s)$, defined on $\partial_c \mathcal{B}_k^h$, using the interpolation

$$f_k^{\text{P}} := \sum_{I=1} N_I(\xi) f_{kI} \quad (40)$$

and define the nodal values f_{kI} as

$$f_{kI} := \frac{\int_{\partial_c \mathcal{B}_{0k}} N_I f_k \, dA_k}{\int_{\partial_c \mathcal{B}_{0k}} N_I \, dA_k} . \quad (41)$$

These f_{kI} correspond to an averaging of $f_k(s)$ over the support width of shape function N_I .⁸ In eq. (41), both denominator and numerator can be determined in an element-wise manner. Clearly, the functions $f_k^{\text{P}}(s)$ and $f_k(s)$ are not equal in general, even at the finite element nodes, i.e. $f_k^{\text{P}}(s_I) = f_{kI} \neq f_k(s_I)$. However, as the FE mesh spacing h approaches zero, N_I approaches the Dirac delta function, so that $f_k^{\text{P}}(s_I) \rightarrow f_k(s_I)$ and

$$f_k^{\text{P}}(s) \rightarrow f_k(s) \quad \text{for } h \rightarrow 0 . \quad (42)$$

This property carries over to the finite element approximation of f_k , denoted f_k^h , as long as $f_k^h \rightarrow f_k$ as $h \rightarrow 0$.⁹ This is the case for the contact pressure considered in the following examples. A formal proof of eq. (42) is included in Appendix B. Property (42) motivates the proposed interpolation scheme.

For the Hermite (Q1CH) enrichment scheme, the post-processing takes the form

$$f_k^{\text{P}} := \sum_I N_I(\xi) f_{kI} + \sum_I H_I(\xi) f'_{kI} . \quad (43)$$

The nodal interpolant f'_{kI} , which expresses the derivative w.r.t. ξ , is constructed from the averaging¹⁰

$$f'_{kI} := \frac{- \int_{\partial_c \mathcal{B}_{0k}} N'_I f_k \, dA_k}{\int_{\partial_c \mathcal{B}_{0k}} N_I \, dA_k} , \quad (44)$$

⁷We first consider the continuous case, i.e. f_k does not depend on the FE discretization.

⁸Only the support area contained in the contact surface $\partial_c \mathcal{B}_k$ is considered.

⁹To satisfy eq. (42), any dependence of f_k^h on h must decay rapidly as $h \rightarrow 0$; see Appendix B.

¹⁰Alternatively, one could consider $N_I f'_k$ in eq. (44), but this is less convenient as $f'_k = f_{k,\xi}$ is usually not readily available.

as it satisfies the property $f_{k,\xi}^p(s_I) = f'_{kI} \rightarrow f_{k,\xi}(s_I)$ as $h \rightarrow 0$. Thus, interpolation (43) also satisfies property (42).

For the examples in Sec. 4, we use interpolations (40) and (43) to construct smooth fields for the contact pressure, contact shear and the surface stretch, i.e we consider

- $p_k := \mathbf{t}_k \cdot \mathbf{n}_p$
- $\tau_k := \mathbf{t}_k \cdot \bar{\mathbf{a}}_p$
- λ_k^s

for f_k in eqs. (41) and (44); see Figs. 7, 8 and 15.

To demonstrate convergence, we examine the effect of the proposed post-processing scheme on the contact pressure of the ironing example of Sec. 4.3. Fig. 3a shows the convergence of the raw contact pressure $p_k = -\epsilon_n g_n$ (according to formulation (6)) and the post-processed contact pressure p_k^p for the Q1CH discretization (defined by (43)). As seen, the post-processed

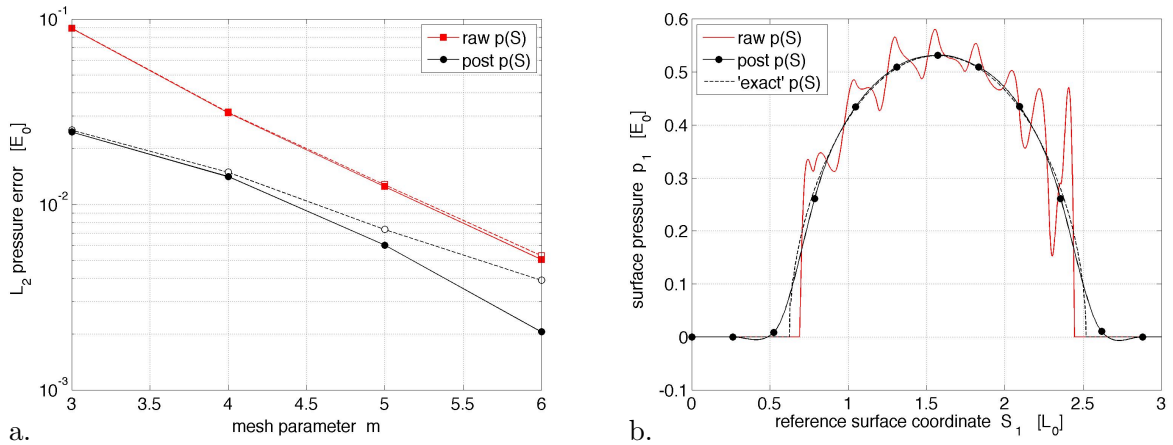


Figure 3: Convergence of the post-processing scheme for the numerical example discussed in Sec. 4.3. Shown is the contact pressure acting on the cylinder. a.: error for increasing mesh density (solid lines: L^2 error w.r.t. post-processed pressure at $m = 7$; dashed lines: L^2 error w.r.t. raw pressure at $m = 7$). b.: accuracy of the raw and post-processed contact pressure (for $m = 3$; dots correspond to FE nodes); ‘exact’ denotes the raw pressure for $m = 7$.

pressure converges faster than the raw pressure. This is due to the smoothing property of the post-processing scheme that is seen in Fig. 3b: The raw pressure oscillates for a coarse FE discretization with large contact penalty (here $\epsilon_n = 1000E_0/L_0$).¹¹ The post-processing scheme gets rid of these oscillations and thus comes very close to the ‘exact’ result. Note, that the oscillations in the raw pressure can only be captured, if sufficiently many quadrature points are used for their evaluation. The FE meshes used in Fig. 3 contain $5 \cdot 2^{2m}$ elements inside the block and $21 \cdot 2^{2m-5}$ elements inside the cylinder (see Fig. 13 for $m = 3$).

¹¹These oscillations, according to eq. (6), reflect the discretization error in the approximation of the normal contact penetration $-g_n$. For comparably large penalty parameters (considered here) and coarse FE discretizations, the contact penetration is very small compared to the element size, so that surface inaccuracies are amplified in the computation of g_n and cause the shown oscillations. As the discretization is refined (while keeping the penalty parameter fixed), the resulting penetration increases compared to the element size. Surface inaccuracies now cause less errors in the computation of g_n and the oscillations in the raw pressure disappear quickly, as the result for $m = 7$ indicates. Due to this rapid decay, eq. (42) holds, which implies that the post-processed pressure, like the raw pressure, converges to the exact contact pressure.

Remark 1: The averaging of eqs. (41) and (44) can also be defined over the current surface $\partial_c \mathcal{B}_k$. This leads to slightly different nodal values, even for linear elements.

Remark 2: One can also consider the traction \mathbf{t}_k directly in eqs. (41) and (44). With this, one can then conceive an alternative definition for the smoothed pressure: Extracting the pressure out of the smoothed traction, instead of smoothing the extracted pressure, as is considered above.

Remark 3: Alternatively, for Q1CH elements, f'_{kI} can also be defined as

$$f'_{kI} := \frac{\frac{15}{4} \int_{\partial_c \mathcal{B}_{0k}} H_I f_k \, dA_k}{\int_{\partial_c \mathcal{B}_{0k}} N_I \, dA_k} . \quad (45)$$

The factor $15/4$, as well as the minus sign in definition (44), are needed in order to reproduce linear functions exactly. Compared to (44), alternative (45) only yields minor differences.

4 Numerical examples

This section discusses several numerical examples that illustrate the performance of the enriched contact formulation for the contact models presented in Sec. 2.

4.1 Frictional ironing problem

4.1.1 Problem setup

As a first example we consider sliding contact between a rigid cylinder (radius L_0) and a deformable block (dimensions $2L_0 \times 10L_0$), as shown in Fig. 4. The example is used to study the

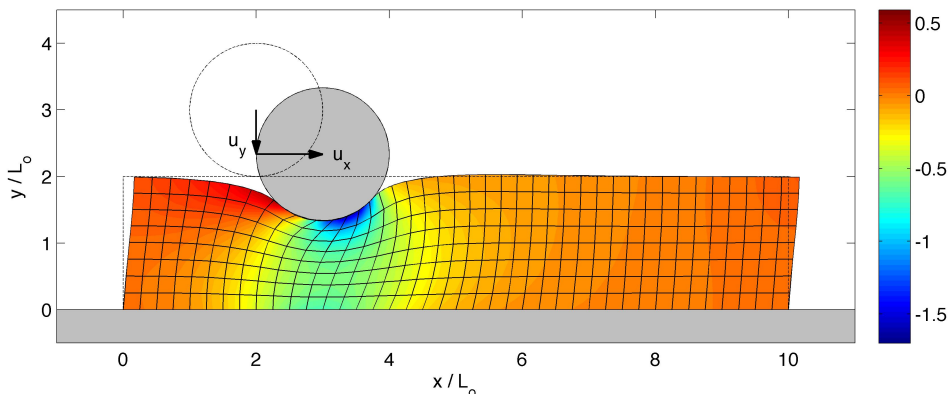


Figure 4: Ironing problem: frictional sliding contact between a rigid cylinder and a soft block. The coloring shows the stress $I_1 = \text{tr } \boldsymbol{\sigma}$ normalized by E .

contact force, contact tractions and the surface stretch as they are obtained from the different enhancement formulations. The example is identical to the frictionless example reported in Sauer (2011), with the only difference that now friction is considered. The bottom of the block is considered fixed, and a periodic boundary condition is applied to the vertical boundaries of the

block. In this case, the contact state remains constant during sliding and the net contact forces P_x and P_y remain constant. The block is modeled by the Neo-Hookean material law (33) using $\nu = 0.3$. E and L_0 are used for normalization and remain unspecified. The contact parameters for normal contact (Sec. 2.1) and friction (Sec. 2.2) are chosen as $\epsilon_n = 100 E/L_0$, $\epsilon_t = 100 E/L_0$ and $\mu = 0.5$. The mesh of Fig. 4, with 4 elements per L_0 and $n_{qp} = 100$ quadrature points per contact element, is used for the following analysis.

4.1.2 Contact forces

Fig. 5 shows the net contact forces P_x and P_y as function of the sliding distance u_x . Shown

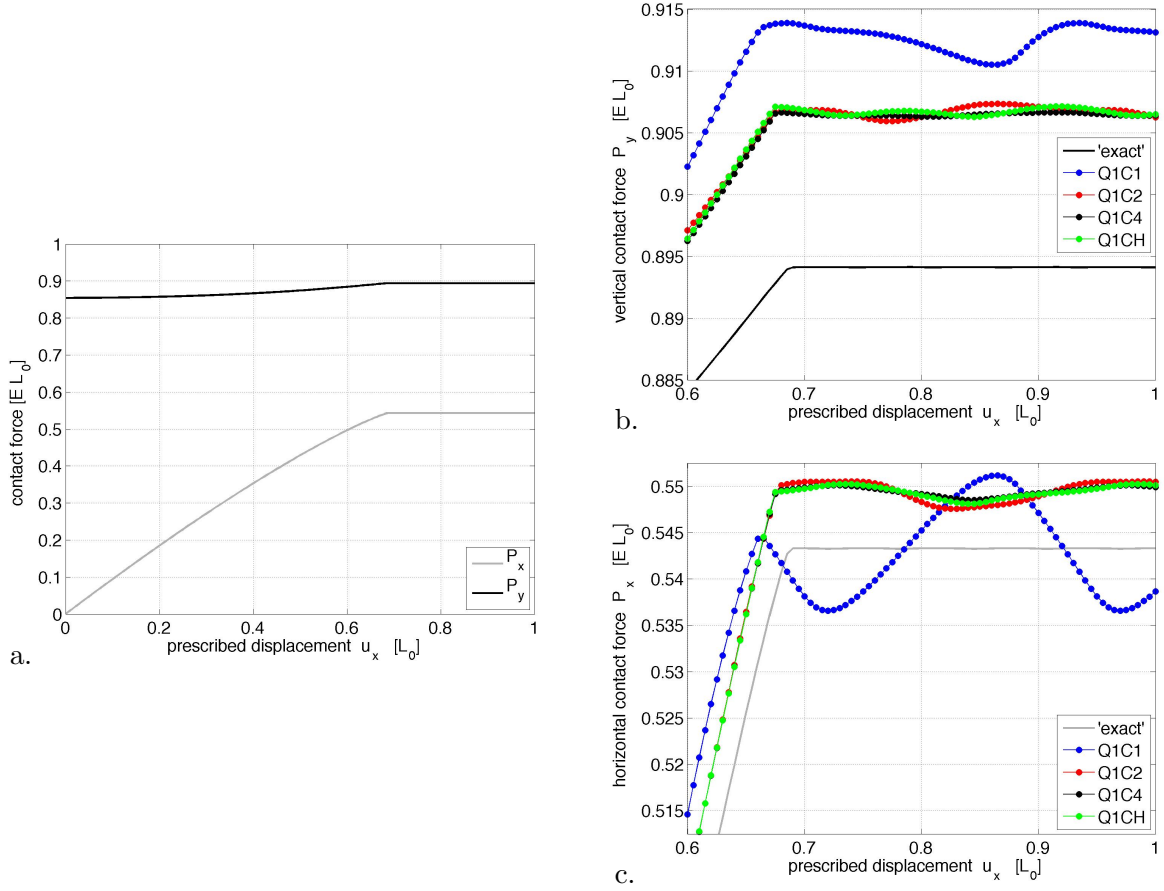


Figure 5: Contact forces P_x and P_y between cylinder and block in dependence of the sliding distance u_x : a.: 'Exact' result; b. & c.: Enlargement showing the different contact formulations.

are the results for the different contact formulations in comparison to the 'exact' result, which is obtained from a very fine mesh (using 32 equidistant finite elements along L_0). The two enlargements show that oscillations are present in all formulations. The period of this is equal to the element length $L_0/4$. The oscillations are very large for Q1C1, and reduced substantially for the enrichments Q1C2, Q1C4 and Q1CH. A quantitative analysis of this is given in Tab. 1. Here,

$$\Delta P_i := \max_{u_x} (P_i) - \min_{u_x} (P_i), \quad i = x, y \quad (46)$$

denotes the oscillation magnitude of forces P_x and P_y . In the table these are reported relative to the 'exact' force values, denoted P_x^{ex} and P_y^{ex} . Compared to the Q1C1 solution, the error

element	$\Delta P_x/P_x^{\text{ex}}$	$\text{dev}(P_x)/P_x^{\text{ex}}$	$\Delta P_y/P_y^{\text{ex}}$	$\text{dev}(P_y)/P_y^{\text{ex}}$
Q1C1	2.6853%	1.4474%	0.3774%	2.2100%
Q1C2	0.5402%	1.3297%	0.1555%	1.4787%
Q1C4	0.2933%	1.2556%	0.0375%	1.4014%
Q1CH	0.3982%	1.2815%	0.0937%	1.4553%

Table 1: Performance of the enhanced contact elements for the frictional ironing example of Fig. 4.

ΔP_x reduces by a factor of 5 for the Q1C2 formulation, by 6.7 for the Q1CH formulation and by 9.2 for the Q1C4 formulations. The error ΔP_y reduces by a factor of 2.4, 4.0 and 10 for the Q1C2, Q1CH and the Q1C4 formulation, respectively. The enhanced contact elements thus achieve a substantial improvement compared to the standard Q1C1 formulation. However, the improvements are not as large as those obtained for the same example considering frictionless contact (Sauer, 2011). The table also reports the maximum deviation

$$\text{dev}(P_i) := \max \left\{ \max_{u_x} (P_i) - P_i^{\text{ex}}, P_i^{\text{ex}} - \min_{u_x} (P_i) \right\}, \quad i = x, y \quad (47)$$

of the oscillatory forces P_x and P_y from the exact values. This error decreases only slightly for P_x , but more significantly for P_y . Essentially, there are still significant errors remaining between the ‘exact’ results and the results for the enhanced contact formulations. These are caused by the inaccuracy of the domain discretization rather than by the contact surface discretization. This can be inferred from the values for $\text{dev}(P_x)$ and $\text{dev}(P_y)$, which change only minimally between the Q1C2, Q1CH and Q1C4 formulation.

Hence, the proposed contact enhancement may not increase the overall accuracy. This should not be held against the technique, as its primary purpose is to increase the accuracy of the contact contribution (34) and thereby stabilizing contact computations, especially for coarse discretizations. Still, the proposed enrichment formulation shows better convergence behavior as was shown in Sauer (2011) and is also seen in Sec. 4.3.

Remark: A possible source of error could be the locking of the Q1 elements used in the domain. It would therefore be useful to combine the new contact elements with locking remedies like enhanced strain formulations (Simo and Armero, 1992).

4.1.3 Contact deformation and stresses

Fig. 6 shows an enlargement of the deformation and stress during sliding. The figure shows large inaccuracies in the surface deformation for Q1C1 elements, but much more accurate results for Q1C2, Q1C4 and Q1CH elements. In case of Q1C4 elements large oscillations appear in the stress field. These also show up in the pressure field (Sec. 4.1.4). For Q1CH elements no such oscillations appear. These elements are highly accurate and, contrary to the other formulations, provide a C^1 -smooth surface representation.

4.1.4 Contact tractions

Fig. 7 shows the contact pressure and shear for the four different contact formulations and the ‘exact’ result obtained with a dense mesh (32 elements along L_0 using Q1CH). The post-processing scheme of Sec. 3.4 is used for these plots. Note the proportionality of $\mu = 0.5$ between τ and p . The Q1C1 formulation provides only a coarse representation of the pressure field. The accuracy is improved for the Q1C2 formulation. However, the pressure turns oscillatory for this

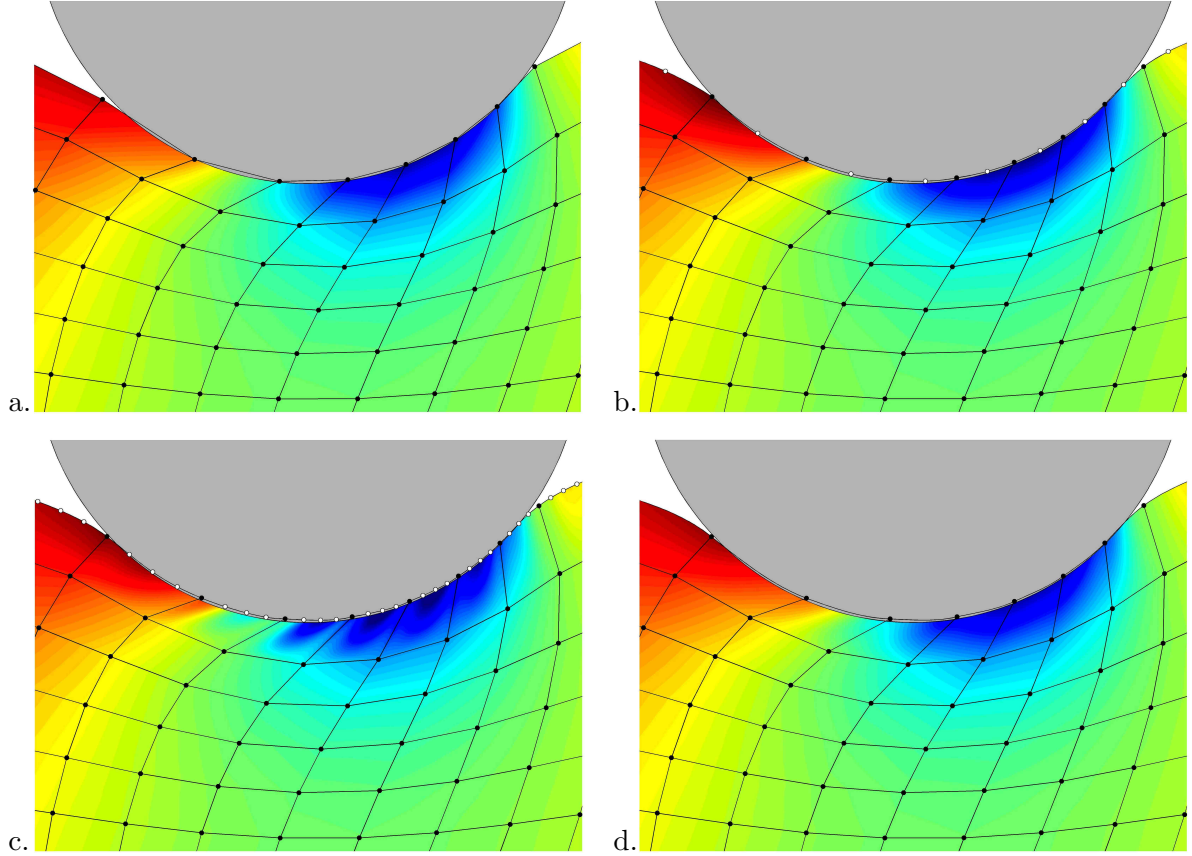


Figure 6: Enlargement of the contact deformation and I_1 stress according to the: a. Q1C1 formulation; b. Q1C2 formulation.; c. Q1C4 formulation; d. Q1CH formulation. The stress coloring is the same as in Fig. 4 (ranging from -1.70 E to 0.59 E).

enhancement. This is even worse for the Q1C4 formulation. The Q1CH formulation, on the other hand, provides a smooth and accurate representation of the contact pressure and shear. According to definition (43) it is even C^1 -continuous. The pressure oscillations caused by high-order Lagrange interpolation (Q1C2 and Q1C4) are similar to those observed by [De Lorenzis et al. \(2011\)](#) and [Temizer et al. \(2011\)](#).

For a detailed analysis of the accuracy of the different formulations let us examine the relative L^2 error norm

$$\|\Delta \bar{p}\|_{L^2} := \sqrt{\frac{1}{|\partial_c \mathcal{B}|} \int_{\partial_c \mathcal{B}} (p_{\text{Q1CX}} - p_{\text{exact}})^2 dA} \quad (48)$$

obtained over the contact area $\partial_c \mathcal{B}$ where $p \neq 0$. These errors are listed in Tab. 2. It can be

element	$\ \Delta \bar{p}\ _{L^2}$
Q1C1	$1.625 \cdot 10^{-3}$
Q1C2	$0.818 \cdot 10^{-3}$
Q1C4	$1.774 \cdot 10^{-3}$
Q1CH	$0.789 \cdot 10^{-3}$

Table 2: L^2 error in the pressure field p according to eq. (48) for the various contact formulations.

seen that formulations Q1C2 and Q1CH achieve a much lower pressure error than formulations

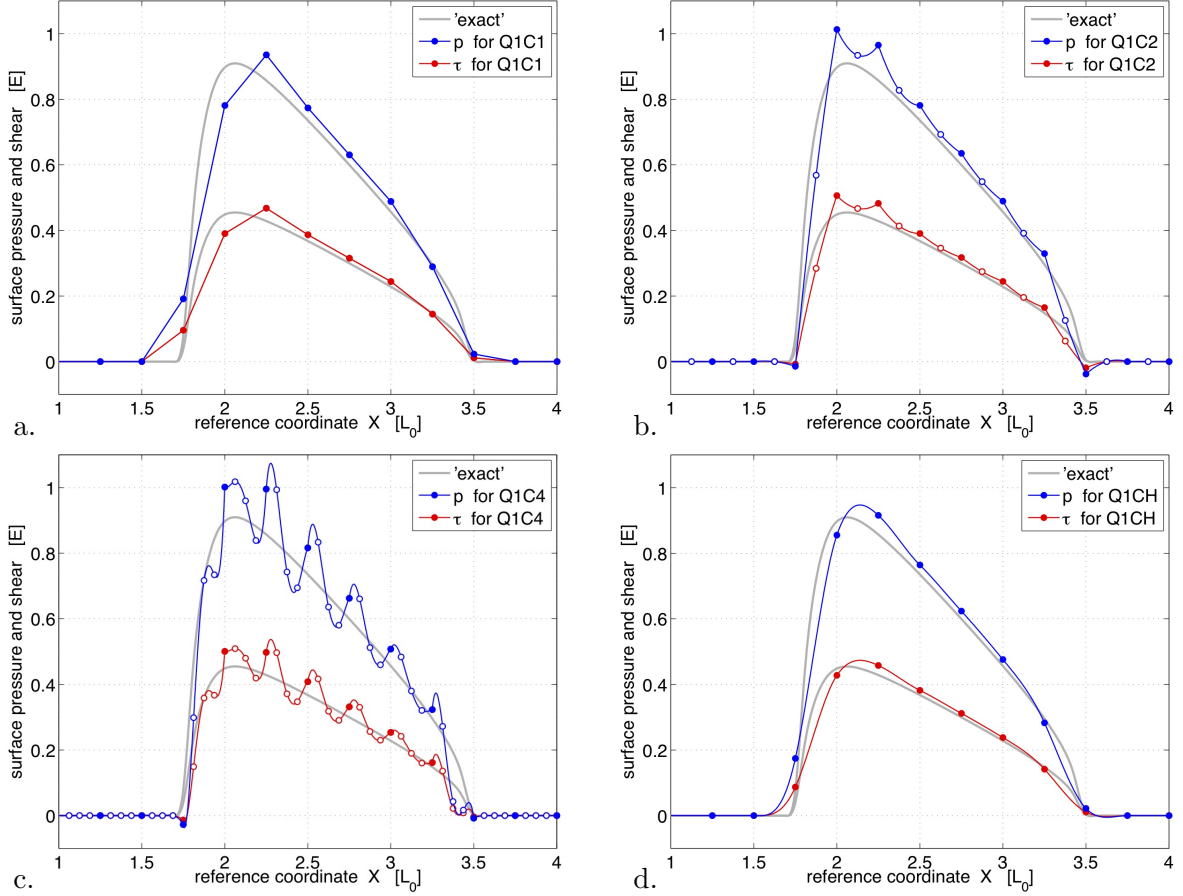


Figure 7: Contact pressure according to the: a. Q1C1 formulation; b. Q1C2 formulation.; c. Q1C4 formulation; d. Q1CH formulation. The filled dots show the pressure at the standard FE nodes, the white dots show the pressure at the enrichment nodes.

Q1C1 and Q1C4.

Remark: During sliding the boundary of the contact surface typically falls within a surface element, which produces approximation errors at those boundaries. These errors decrease with the proposed enrichment formulations as Fig. 7 shows. A further accuracy gain can be expected from considering nodal relocation strategies (Franke et al., 2010).

4.1.5 Surface stretch

We finally examine the surface stretch λ^s , defined in eq. (4). This is shown in Fig. 8. The post-processing scheme of Sec. 3.4 is used. Conclusions similar to those for the contact pressure can be drawn: Q1C1 is quite inaccurate, Q1C2 and Q1C4 are more accurate but oscillatory, and Q1CH is the most accurate and also C^1 -smooth. The stretch is important for the accurate integration of the contact tractions according to eq. (34). It is seen that extreme surface stretch values occur in the contact zone.

Due to the pressure and stretch oscillations of the Q1C4 formulation, we will disregard this technique in the following examples, and focus on formulations Q1C1, Q1C2 and Q1CH.

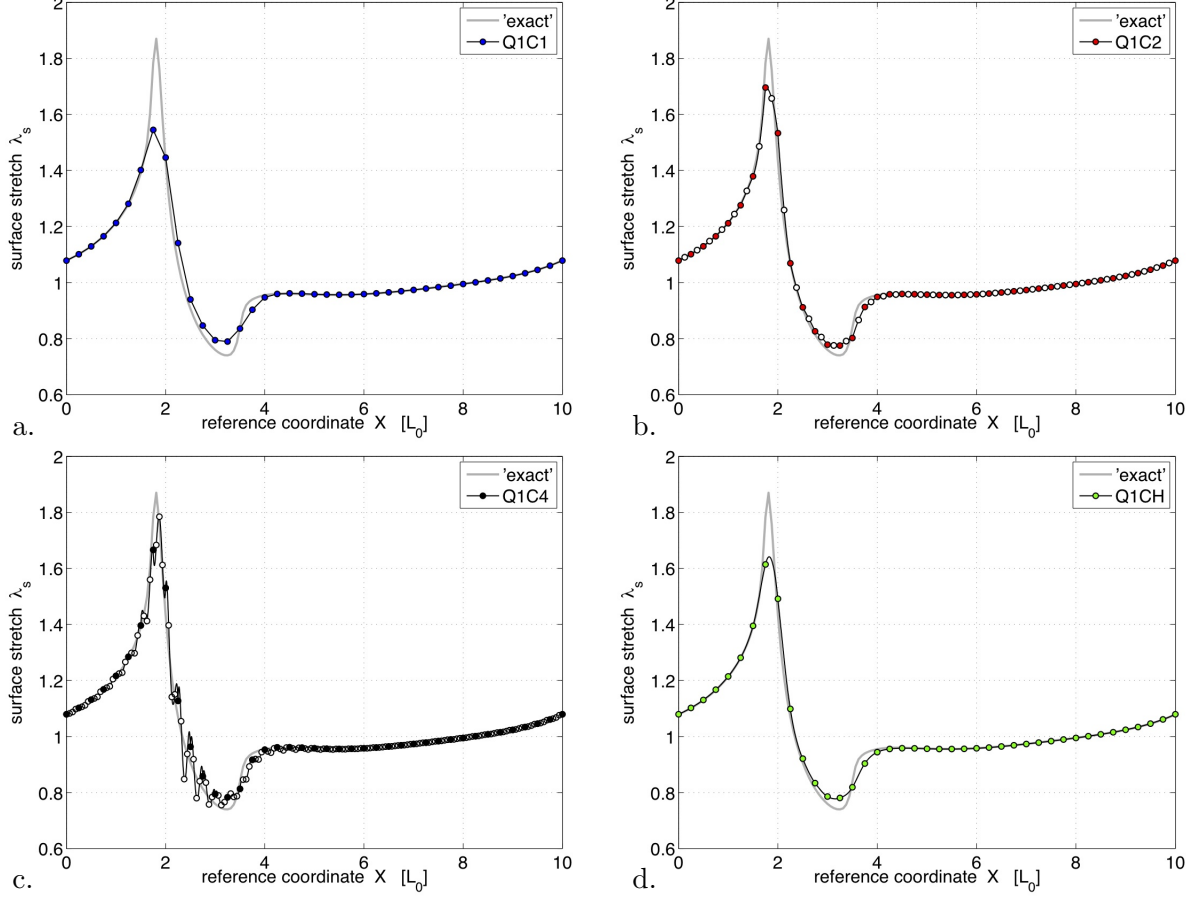


Figure 8: Contact surface stretch according to the: a. Q1C1 formulation; b. Q1C2 formulation.; c. Q1C4 formulation; d. Q1CH formulation. The dark dots show the stretch at the standard FE nodes, the white dots show the stretch at the enrichment nodes.

4.2 Debonding of two flexible strips

The second example considers the delamination of two flexible strips, a problem also known as the double cantilever beam (DCB) peeling problem. The setup of the example is shown in Fig. 9. For both strips the Neo-Hookean material model (33) is considered with $E_2 = 3E_0$, $E_1 = E_0$

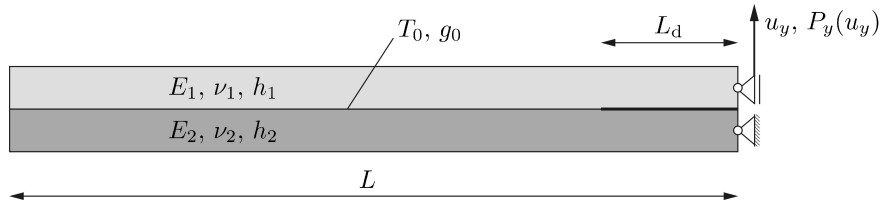


Figure 9: Double strip peeling problem: Initial geometry and boundary conditions.

and $\nu_1 = \nu_2 = 0.3$. The cohesive zone model from Sec. 2.3 is considered to describe debonding. This model offers only weak resistance to penetration. Therefore the penalty method (Sec. 2.1) is considered additionally to counter penetration. Instead of expression (6), we now use the

quadratic force law

$$\mathbf{t}_k = \begin{cases} \epsilon_n g_n^2 \mathbf{n}_p & \text{for } g_n < 0 \\ \mathbf{0} & \text{for } g_n \geq 0 \end{cases} \quad (49)$$

to get a smooth transition between penetration and separation. For the following computations the model parameters $T_0 = 0.2 E_0$, $g_0 = 0.05 L_0$ and $\epsilon_n = 50 E_0/L_0$ are used. The strip dimensions are taken as $L = 20 L_0$, $h_1 = h_2 = L_0$ and $L_d = 5 L_0$. This last parameter denotes an initial debonding length. Further delamination is induced by the applied vertical displacement u_y . This leads to the peeling behavior shown in Fig. 10. The coloring shows the

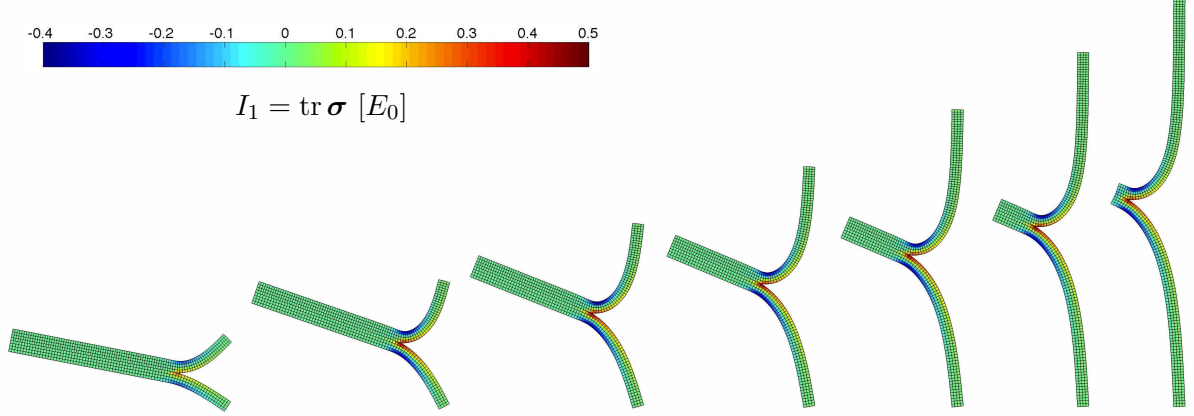


Figure 10: DCB peeling: Strip deformation during peeling. Snap-shots shown at $u_y = 5, 10, 15, 20, 25, 30$ and $34.65 L_0$.

stress $I_1 = \text{tr } \boldsymbol{\sigma}$ during peeling. Due to the different strip stiffness, the strips rotate during deformation and therefore tangential peeling tractions are present in the delamination zone. As Fig. 10 and 12 show, a non-conforming finite element mesh is used to test the computational performance. The two strips are discretized with 96×4 elements (upper strip) and 80×4 elements (lower strip).

The example is computed with elements types Q1C1, Q1C2 and Q1CH. Fig. 11 shows the load-displacement curve $P_y(u_y)$ during peeling. The enlargement shows that oscillations occur

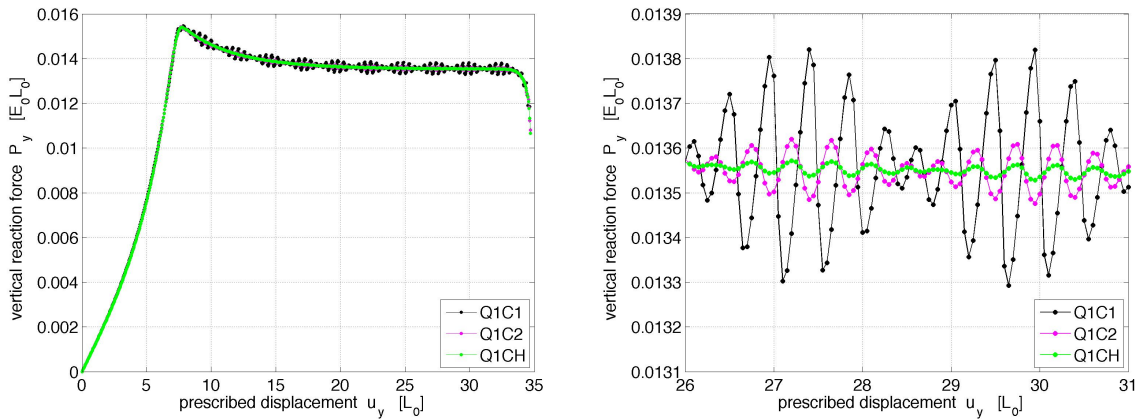


Figure 11: DCB peeling: load displacement curve: entire view (left); zoomed view (right).

for all three formulations. These oscillations are shown in table 3. Compared to the standard

element	ΔP_y
Q1C1	$5.3 \cdot 10^{-4}$
Q1C2	$1.3 \cdot 10^{-4}$
Q1CH	$3.5 \cdot 10^{-5}$

Table 3: Maximum oscillation errors in P_y , normalized by $E_0 L_0$, for the various contact formulations.

Q1C1 formulation, the oscillations reduce by a factor of 4 for the Q1C2 enrichment and even 15 for the Q1CH enrichment. Interestingly, these are the same factors as obtained for the peeling example of Sauer (2011), which considers a deformable strip on a rigid substrate.

Fig. 12 shows an enlargement of the deformation at $u_y = 10 L_0$. In contrast to Q1C1, Q1CH

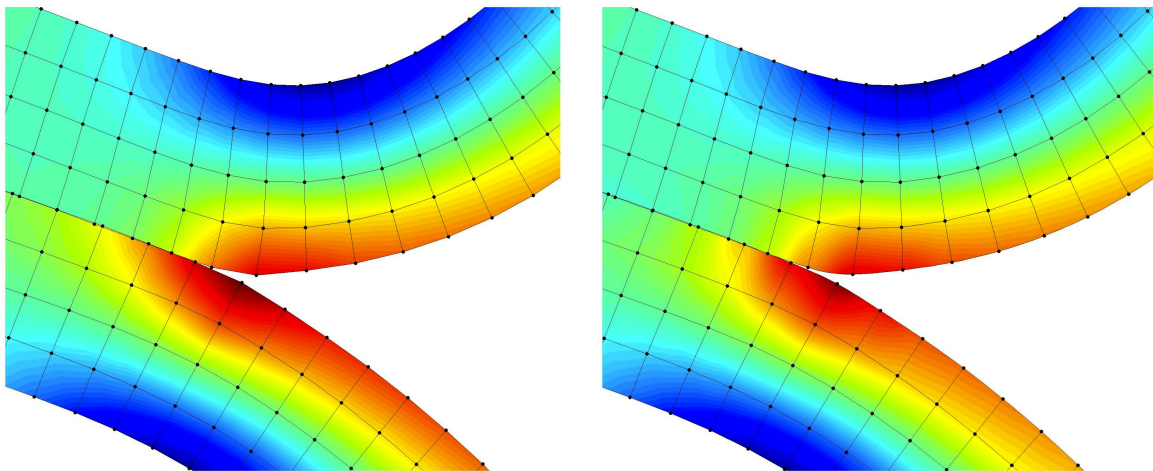


Figure 12: DCB peeling: deformation at $u_y = 10 L_0$. Q1C1 result (left); Q1CH result (right).

achieves a smooth surface representation. This is essentially the reason why the peeling force P_y is computed much more accurately for the Q1CH formulation.

4.3 Frictionless ironing between deformable bodies

The third example re-examines the ironing problem, now considering both bodies as deformable, but restricted to the case of frictionless contact. A half-cylinder \mathcal{B}_1 , with radius L_0 , is pressed into an elastic block \mathcal{B}_2 and then moved horizontally across, as is shown in Fig. 13. The size of the block is $2L_0 \times 10L_0$. The bottom surface of the block is fixed, and a periodic boundary condition is applied at the two vertical boundaries. In this case, the horizontal contact force P_x vanishes in theory. The Neo-Hooke material law (33) is used with $E_1 = 3E_0$, $E_2 = E_0$, and $\nu_1 = \nu_2 = 0.3$.

Contact is computed with the penalty method for frictionless contact (Sec. 2.1) using the two-half-pass algorithm (Sauer and De Lorenzis, 2012). In this reference, the same example was considered to compare the two-half-pass algorithm to a classical full-pass algorithms. Here we are interested in analyzing the proposed contact enrichment. In the following computations two penalty parameters are considered: $\epsilon_n = 100 E_0/L_0$ and $\epsilon_n = 1000 E_0/L_0$. Sliding friction is not considered here, since the two-half-pass algorithm has not yet been formulated for frictional contact.

Four finite elements per L_0 are used, and up to $n_{qp} = 200$ equidistant quadrature points are

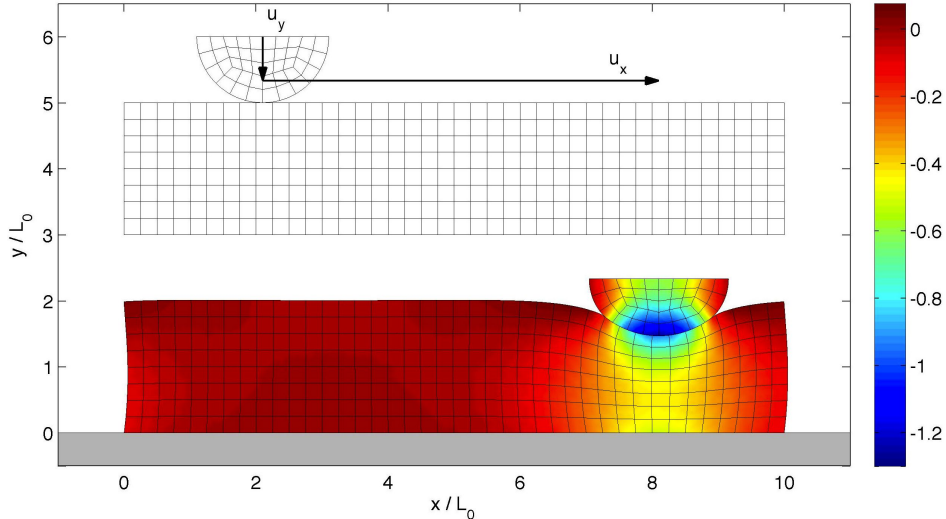


Figure 13: Frictionless ironing between deformable solids: Initial configuration and deformed configuration. The coloring shows the stress $I_1 = \text{tr } \boldsymbol{\sigma}$ normalized by E_0 .

used for the integration of contact integral (34). It is emphasized, that large n_{qp} are only used to obtain highly accurate results for comparison. This is particularly useful for Q1C1, where the jumps of the surface normal \boldsymbol{n} at the finite element nodes affect the evaluation of the contact forces.¹² The influence of single jumps decreases as n_{qp} increases. Large n_{qp} are not required for computational robustness.

Fig. 14 shows a comparison between Q1C1 and Q1CH solutions during sliding for $\epsilon_n = 1000 E_0/L_0$ and $n_{\text{qp}} = 200$. For these parameters, the contact penetration is less than $0.0006 L_0$ (taken from Q1CH), which corresponds to less than 2.5 thousands of $L_0/4$, the reference element length of the block. As the figure shows, Q1C1 gives quite poor results: unphysical lateral deformations appear in the block in order to adjust to the cylinder surface. Also, the convergence behavior for Q1C1 is extremely poor, taking up to 35 Newton iteration steps per load step (50 load steps per L_0 were used for dense output).¹³ On the other hand, the Q1CH formulation gives very good results, which are obtained with a maximum of 6 Newton steps. The problem of over-constraining is completely absent here, even though ϵ_n and n_{qp} are very large.

Fig. 15 shows the contact pressure according to Sec. 3.4, for the same ϵ_n and n_{qp} . Each plot shows two curves: the pressure acting on the cylinder (\mathcal{B}_1) and the pressure acting on the block (\mathcal{B}_2). As seen, there is an excellent agreement between the two pressure fields, although this is not enforced a-priori within formulation (34): The tractions \boldsymbol{t}_1 and \boldsymbol{t}_2 are computed independently, without enforcing any continuity! Note that the contact pressure is much smoother for the Q1CH formulation. According to definition (43) they are C^1 -continuous themselves.

Fig. 16 shows the global contact forces during sliding. Due to the FE discretization, these oscillate with the period $L_0/4$. These oscillations are spurious, and can thus be taken as an error measure for the different enrichment formulations. As noted in Fig. 15, each case (Q1C1, Q1C2 and Q1CH) produces two contact forces: \boldsymbol{P}_1 , acting on \mathcal{B}_1 , and \boldsymbol{P}_2 , acting on \mathcal{B}_2 . Their difference is a measure for the error in contact formulation (34). The figure shows that this

¹²An averaging of \boldsymbol{n} , as proposed by Yang et al. (2005) was not considered.

¹³The active set is considered frozen until a certain threshold is reached during the equilibrium iteration. During this freeze, the system is severely over-constrained, which leads to the unphysical tangential deformations seen in the figure.

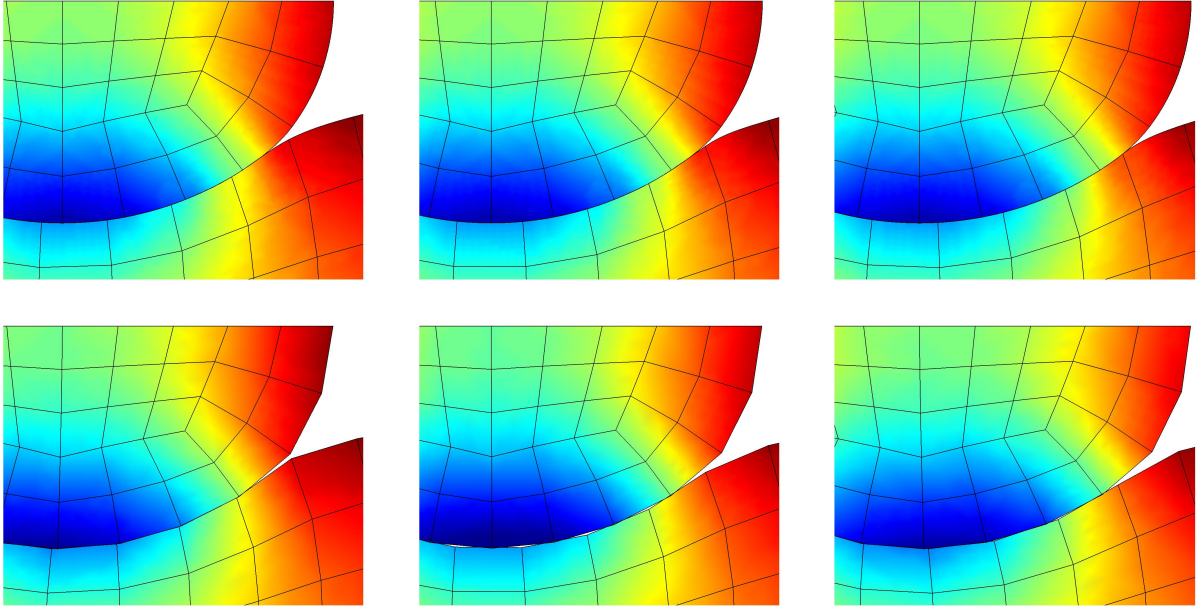


Figure 14: Ironing snapshots for Q1C1 (bottom row) and Q1CH (top row) for $\epsilon_n = 1000 E_0/L_0$. The coloring shows I_1 and is the same as in Fig. 13. The snapshots are taken at $u_x = 0.23 L_0$, $u_x = 0.28 L_0$ and $u_x = 0.33 L_0$.

error is larger for Q1C1 than for Q1C2 and Q1CH. The error between \mathbf{P}_1 and \mathbf{P}_2 decreases as the penalty parameter increases. On the other hand, the increase in ϵ_n leads to an increase in the oscillation error.

Tab. 4 shows the oscillation error in P_x and P_y for increasing penalty parameters. Looking

element	$\Delta \bar{P}_x$		$\Delta \bar{P}_y$	
	$\bar{\epsilon}_n = 100$	$\bar{\epsilon}_n = 1000$	$\bar{\epsilon}_n = 100$	$\bar{\epsilon}_n = 1000$
Q1C1	12.2e-3 (100%)	57.7e-3 (100%)	9.7e-3 (100%)	12.0e-3 (100%)
Q1C2	0.74e-3 (6.1%)	1.15e-3 (2.0%)	4.5e-3 (46%)	1.56e-3 (13%)
Q1CH	0.77e-3 (6.3%)	1.24e-3 (2.1%)	4.0e-3 (41%)	1.21e-3 (10%)

Table 4: Maximum oscillation errors in P_x and P_y for the various contact formulations. Here, $\bar{\epsilon}_n = \epsilon_n L_0/E_0$ and $\Delta \bar{P} = (\max P - \min P)/E_0/L_0$, where the max and min are taken over u_x .

at each column one can see that the errors decrease substantially for the Q1C2 and Q1CH formulation. The decrease is particularly large for $\bar{\epsilon}_n = 1000$, where one finds error reductions by a factor of 50 (Q1C2) and 47 (Q1CH) for P_x and 7.7 (Q1C2) and 9.9 (Q1CH) for P_y . Comparing the P_x columns for $\bar{\epsilon}_n = 100$ and $\bar{\epsilon}_n = 1000$, one sees that increasing the penalty parameter increases the error. This increase is very large for Q1C1, but much less for Q1C2 and Q1CH. Comparing the P_y columns, one finds an error increase for Q1C1 and a major error decrease for Q1C2 and Q1CH.

Finally, Fig. 17 shows the convergence behavior for the refinement of the FE discretizations. Here, the maximum of $|P_x|$ and the maximum and minimum of P_y are shown, and $n_y = 2^m$ is the number of elements along the height of the block ($m = 3$ is the mesh shown in Fig. 13). For an increase of m by 1, each element is subdivided into 4 smaller elements. As seen, the imbalances in P_x and P_y vanish for increasing mesh refinement. This is in accordance with the

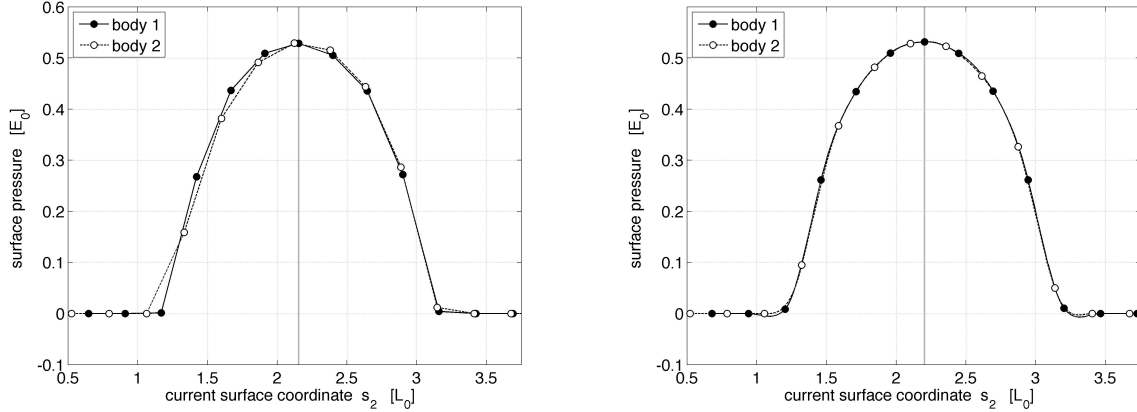


Figure 15: Contact pressure at $u_x = 0$ for $\epsilon_n = 1000 E_0/L_0$ and $n_{qp} = 200$ according to the Q1C1 discretization (left) and the Q1CH discretization (right).

properties of the two-half-pass algorithm (Sauer and De Lorenzis, 2012). Fig. 17 also shows that the errors in both force components are much lower for Q1CH than for Q1C1. Overall, Q1CH converges faster. Due to its proportionality to E_0/L_0 the penalty parameter is taken as 1000, 2000 and 4000 for the three meshes $m = 3$, $m = 4$, $m = 5$ in Fig. 17.

In summary, we again find that the proposed contact enrichment formulations provide a huge gain in accuracy and robustness.

5 Conclusion

This paper extends the enriched contact formulation of Sauer (2011) to friction and deformable-deformable contact. The formulation uses local finite element enrichment to increase the accuracy of the contact integrals. It therefore directly affects both the evaluation of the contact kinematics, based on closest point projection, and the integration of the contact energy over the contact surface. Here, the contact equations are enforced at the quadrature points using the two-half-pass algorithm of Sauer and De Lorenzis (2012). The enrichment considered here is based on high-order Lagrange and Hermite interpolation. The second offers C^1 -smooth contact surface representations that are free from the oscillations troubling the high-order Lagrange enrichment Q1C4. Therefore this approach seems less useful than the other formulations. The enrichment formulations are characterized by compact support, which leads to compact coupling entries in the resulting contact tangent matrix.

The paper also presents a post-processing scheme for contact quantities like the contact pressure. The procedure is based on intra-element averaging. For Hermite enrichment highly accurate, C^1 -smooth pressure distributions are thus obtained.

Several numerical examples are presented to illustrate the improved behavior of the enrichment strategies. As for the simpler examples of Sauer (2011), the enrichment leads to a major gain in accuracy and robustness.

For the future several extensions are planned. One is the development of NURBS based contact enrichment approaches. These also allow the straight forward extension to 3D contact enrichment. Another extension is the study of friction between two deformable bodies. Therefore, the contact formulation of Sauer and De Lorenzis (2012) is currently being extended to frictional contact.

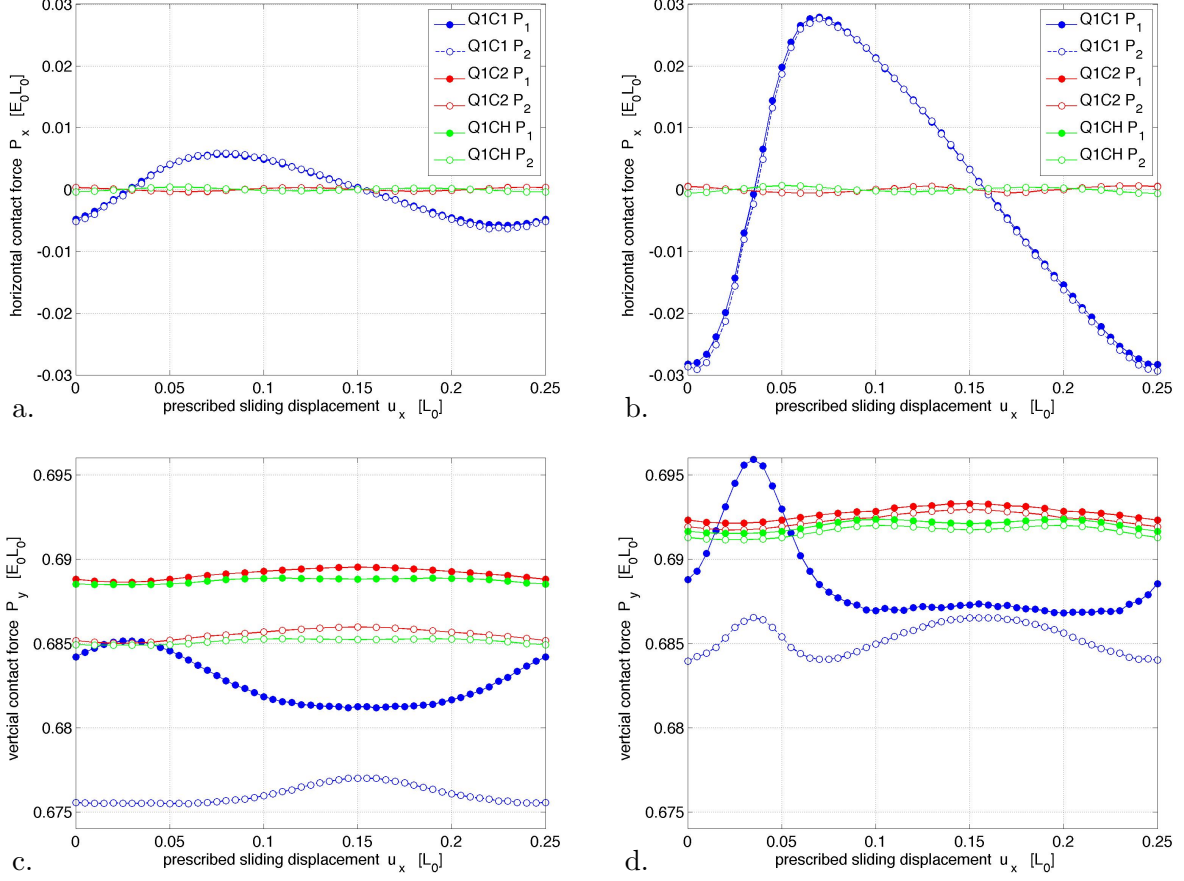


Figure 16: Influence of the penalty parameter on the net contact forces P_x and P_y : a. & c.: $\epsilon_n = 100 E_0/L_0$; b. & d.: $\epsilon_n = 1000 E_0/L_0$. P_k ($k = 1, 2$) denotes the force on \mathcal{B}_k .

A Contact tangent matrix

This appendix provides the 2D tangent matrices for the three contact formulations used in the examples above. All contact quantities are evaluated in the current configuration and therefore need to be linearized there. For further details see also [Sauer and De Lorenzis \(2012\)](#).

According to eq. (34), the tangent matrices associated with the elemental contact force vector \mathbf{f}_{ck}^e take the form

$$\begin{aligned} \mathbf{k}_{ckk}^e &= - \int_{\Gamma_k^e} \mathbf{N}_k^T \frac{\partial \mathbf{t}_k}{\partial \mathbf{u}_k^e} da_k - \int_{\Gamma_k^e} \mathbf{N}_k^T \mathbf{t}_k \otimes \frac{\partial da_k}{\partial \mathbf{u}_k^e} , \\ \mathbf{k}_{ckl}^e &= - \int_{\Gamma_k^e} \mathbf{N}_k^T \frac{\partial \mathbf{t}_k}{\partial \mathbf{u}_l^e} da_k , \end{aligned} \quad (50)$$

where

$$\frac{\partial \mathbf{t}_k}{\partial \mathbf{u}_k^e} = \frac{\partial \mathbf{t}_k}{\partial \mathbf{x}_k} \mathbf{N}_k . \quad (51)$$

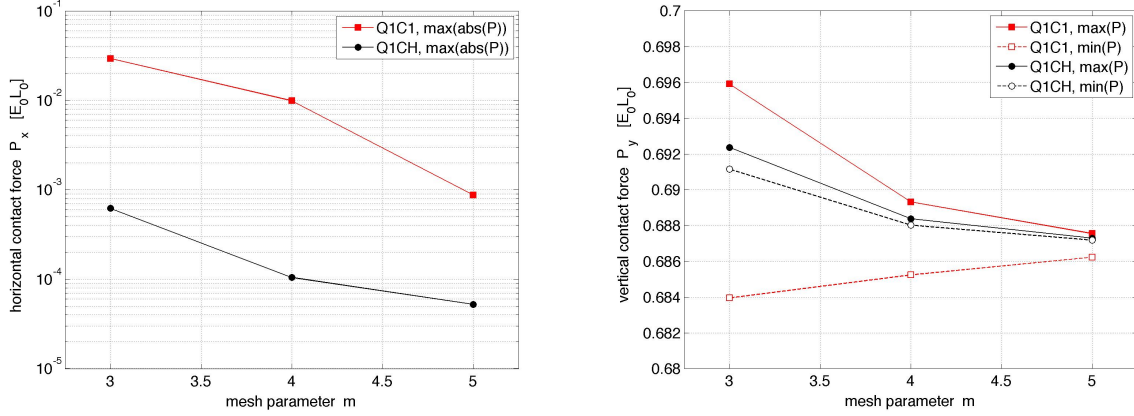


Figure 17: Ironing problem: Convergence of net contact forces P_x (left) and P_y (right) for the Q1C1 and Q1CH formulation.

1. For the normal contact formulation based on the penalty method (Sec. 2.1) we find

$$\begin{aligned} \frac{\partial \mathbf{t}_k}{\partial \mathbf{x}_k} &= p'_k \mathbf{n}_p \otimes \mathbf{n}_p + p_k \frac{\partial \mathbf{n}_p}{\partial \mathbf{x}_k}, \\ \frac{\partial \mathbf{t}_k}{\partial \mathbf{u}_\ell^e} &= -p'_k \mathbf{n}_p \otimes \mathbf{n}_p \mathbf{N}_\ell + p_k \frac{\partial \mathbf{n}_p}{\partial \mathbf{u}_\ell^e}, \end{aligned} \quad (52)$$

with $p'_k = \partial p_k / \partial g_n = -\epsilon_n$ and

$$\begin{aligned} \frac{\partial \mathbf{n}_p}{\partial \mathbf{x}_k} &= \frac{1}{g_n} \left[\mathbf{I} - \mathbf{n}_p \otimes \mathbf{n}_p - c^{11} \mathbf{a}_p \otimes \mathbf{a}_p \right], \\ \frac{\partial \mathbf{n}_p}{\partial \mathbf{u}_\ell^e} &= -\frac{1}{g_n} \left[\mathbf{I} - \mathbf{n}_p \otimes \mathbf{n}_p - c^{11} \mathbf{a}_p \otimes \mathbf{a}_p \right] \mathbf{N}_\ell(\boldsymbol{\xi}_p) - c^{11} \mathbf{a}_p \otimes \mathbf{n}_p \mathbf{N}_{\ell, \xi}(\boldsymbol{\xi}_p), \end{aligned} \quad (53)$$

with $c^{11} = 1/a_{11}/(1 - g_n \kappa_p)$ and $a_{11} = \mathbf{a}_p \cdot \mathbf{a}_p =: \hat{a}_p^2$, see Sauer and De Lorenzis (2012). Here

$$\kappa_p = \mathbf{n}_p \cdot \frac{\partial \bar{\mathbf{a}}_p}{\partial g_t} \quad (54)$$

denotes the curvature of $\partial \mathcal{B}_\ell$ at \mathbf{x}_p . For a parameterized surface representation, κ_p can be easily evaluated from eq. (36). Eq. (53) contains the special cases: (i) projection onto a flat surface ($\kappa_p = 0$), and (ii) projection onto a corner node ($\kappa_p = \infty$). Note that for (i),

$$\frac{\partial \mathbf{n}_p}{\partial \mathbf{x}_k} = \mathbf{0}. \quad (55)$$

Further, from eq. (4) and (38), we have

$$\frac{\partial da_k}{\partial \mathbf{u}_k^e} = \frac{\partial \lambda_k^s}{\partial \mathbf{u}_k^e} dA_k = \frac{1}{\hat{A}_k} \frac{\partial \hat{a}_k}{\partial \mathbf{u}_k^e} dA_k. \quad (56)$$

From the definition $\hat{a}_k := \sqrt{\mathbf{a}_k \cdot \mathbf{a}_k}$ and from eq. (36) we find

$$\frac{\partial \hat{a}_k}{\partial \mathbf{x}_I} = \frac{\partial \hat{a}_k}{\partial \mathbf{a}_k} \frac{\partial \mathbf{a}_k}{\partial \mathbf{x}_I^k} = \bar{\mathbf{a}}_k N_{I, \xi}, \quad (57)$$

and thus

$$\frac{\partial \hat{a}_k}{\partial \mathbf{u}_k^e} = \bar{\mathbf{a}}_k \mathbf{N}_{k,\xi} , \quad (58)$$

so that

$$\frac{\partial da_k}{\partial \mathbf{u}_k^e} = \frac{1}{\hat{a}_k} \bar{\mathbf{a}}_k \mathbf{N}_{k,\xi} da_k . \quad (59)$$

2. For frictional contact (Sec. 2.2) we have the additional, tangential traction $\mathbf{t}_k^t = \tau_k \bar{\mathbf{a}}_p$. We discuss here the case for frictional contact with a rigid neighbor. In this case the tangent matrix is fully specified by eqs. (50a) and (51). According to eq. (22) we find for sticking,

$$\frac{\partial \mathbf{t}_k^t}{\partial \mathbf{x}_k} = \frac{\partial \tau_k^{\text{trial}}}{\partial g_t} \bar{\mathbf{a}}_p \otimes \frac{\partial g_t}{\partial \mathbf{x}_k} + \tau_k^{\text{trial}} \frac{\partial \bar{\mathbf{a}}_p}{\partial g_t} \otimes \frac{\partial g_t}{\partial \mathbf{x}_k} . \quad (60)$$

Here we have

$$\frac{\partial g_t}{\partial \mathbf{x}_k} = \hat{a}_p \frac{\partial \xi_p}{\partial \mathbf{x}_k} = \hat{a}_p c^{11} \mathbf{a}_p \quad (61)$$

(Sauer and De Lorenzis, 2012). We further find

$$\frac{\partial \bar{\mathbf{a}}_p}{\partial g_t} = \kappa_p \mathbf{n}_p \quad (62)$$

from eq. (54) and from the fact that $\bar{\mathbf{a}}_p \cdot \frac{\partial \bar{\mathbf{a}}_p}{\partial g_t} = 0$. Together this gives

$$\frac{\partial \mathbf{t}_k^t}{\partial \mathbf{x}_k} = -\epsilon_t c^{11} \mathbf{a}_p \otimes \mathbf{a}_p + \tau_k^{\text{trial}} \kappa_p \hat{a}_p c^{11} \mathbf{n}_p \otimes \mathbf{a}_p \quad (63)$$

for sticking. For sliding we find

$$\frac{\partial \mathbf{t}_k^t}{\partial \mathbf{x}_k} = \mu \bar{\tau}_k^{\text{trial}} \bar{\mathbf{a}}_p \otimes \frac{\partial p_k}{\partial \mathbf{x}_k} + \mu p_k \bar{\mathbf{a}}_p \otimes \frac{\partial \bar{\tau}_k^{\text{trial}}}{\partial \mathbf{x}_k} + \mu p_k \bar{\tau}_k^{\text{trial}} \frac{\partial \bar{\mathbf{a}}_p}{\partial g_t} \otimes \frac{\partial g_t}{\partial \mathbf{x}_k} , \quad (64)$$

according to eq. (23). The last term is discussed above. The second term vanishes, since $\bar{\tau}_k^{\text{trial}}$ is either equal to 1 or -1 during a sliding increment. For the first term we have $\partial p_k / \partial \mathbf{x}_k = p'_k \mathbf{n}_p$. In total, we thus have

$$\frac{\partial \mathbf{t}_k^t}{\partial \mathbf{x}_k} = -\epsilon_n \mu \bar{\tau}_k^{\text{trial}} \bar{\mathbf{a}}_p \otimes \mathbf{n}_p + \tau_k \kappa_p \hat{a}_p c^{11} \mathbf{n}_p \otimes \mathbf{a}_p \quad (65)$$

for sliding.

3. Cohesive zone model (Sec. 2.3): Writing $\mathbf{T}_k = T_k \bar{\mathbf{g}}$ we now have

$$\begin{aligned} \mathbf{k}_{cck}^e &= - \int_{\Gamma_k^e} \mathbf{N}_k^T \frac{\partial \mathbf{T}_k}{\partial \mathbf{x}_k} \mathbf{N}_k dA_k , \\ \mathbf{k}_{ckl}^e &= - \int_{\Gamma_k^e} \mathbf{N}_k^T \frac{\partial \mathbf{T}_k}{\partial \mathbf{x}_p^0} \mathbf{N}_l dA_k . \end{aligned} \quad (66)$$

with

$$\begin{aligned} \frac{\partial \mathbf{T}_k}{\partial \mathbf{x}_k} &= \frac{\partial T_k}{\partial g} \mathbf{n}_p \otimes \mathbf{n}_p + T_k \frac{\partial \bar{\mathbf{g}}}{\partial \mathbf{x}_k} , \\ \frac{\partial \mathbf{T}_k}{\partial \mathbf{x}_p^0} &= -T'_k \mathbf{n}_p \otimes \mathbf{n}_p + T_k \frac{\partial \bar{\mathbf{g}}}{\partial \mathbf{x}_p^0} , \end{aligned} \quad (67)$$

and

$$\frac{\partial \bar{\mathbf{g}}}{\partial \mathbf{x}_k} = - \frac{\partial \bar{\mathbf{g}}}{\partial \mathbf{x}_p^0} = \frac{1}{g} (\mathbf{I} - \bar{\mathbf{g}} \otimes \bar{\mathbf{g}}) . \quad (68)$$

B Convergence proof for the proposed post-processing scheme

This appendix provides a proof for eq. (42). For brevity, index k is omitted. Consider a function $f(s)$ along s that is independent of h , where h is the distance between FE nodes.¹⁴ Eq. (42) is satisfied if the approximate nodal values $f_I := f^p(s_I)$ are equal to $f(s_I)$ at all nodal positions s_I . For the considered element classes, the area beneath shape function $N_I(s)$ is proportional to h , i.e. we can write

$$\int_{\partial_c \mathcal{B}} N_I(s) ds = ch, \quad c > 0. \quad (69)$$

(For Q1C1 and Q1CH we have $c = 1$.) According to definition (41), considered here over the current area, we then find

$$\lim_{h \rightarrow 0} f_I = \lim_{h \rightarrow 0} \frac{1}{ch} \int_{\partial_c \mathcal{B}} N_I(s) f(s) ds. \quad (70)$$

As $h \rightarrow 0$, $N_I(s)/h$ approaches a Dirac delta function located at s_I . We thus have

$$\lim_{h \rightarrow 0} \frac{N_I(s)}{h} f(s) = \lim_{h \rightarrow 0} \frac{N_I(s)}{h} f(s_I), \quad (71)$$

since $f(s)$ approaches the constant $f(s_I)$ within the support width of $N_I(s)$. Therefore

$$\lim_{h \rightarrow 0} f_I = \lim_{h \rightarrow 0} \frac{1}{ch} \int_{\partial_c \mathcal{B}} N_I(s) ds f(s_I) = f(s_I). \quad (72)$$

□

Acknowledgements

The author is grateful to the German Research Foundation (DFG) for supporting this research under projects SA1822/5-1 and GSC 111.

References

- Crisfield, M. A. and Alfano, G. (2002). Adaptive hierarchical enrichment for delamination fracture using a decohesive zone model. *Int. J. Numer. Meth. Engrg.*, **54**(9):1369–1390.
- De Lorenzis, L., Temizer, I., Wriggers, P., and Zavarise, G. (2011). A large deformation frictional contact formulation using NURBS-based isogeometric analysis. *Int. J. Numer. Meth. Engrg.*, **87**:1278–1300.
- El-Abbasi, N., Meguid, S. A., and Czekanski, A. (2001). On the modeling of smooth contact surfaces using cubic splines. *Int. J. Numer. Meth. Engrg.*, **50**:953–967.
- Fischer, K. A. and Wriggers, P. (2005). Frictionless 2D contact formulations for finite deformations based on the mortar method. *Comput. Mech.*, **36**:226–244.
- Franke, D., Düster, A., Nübel, V., and Rank, E. (2010). A comparison of the h-, p-, hp- and rp-version of the FEM for the solution of the 2D Hertzian contact problem. *Comput. Mech.*, **45**:513–522.

¹⁴It is sufficient to require that any dependency of f on h decays faster than h as $h \rightarrow 0$. One can then write $f = f_0 + f_h$ where $f_0 = f$ at $h = 0$ and f_h is the decaying, h -dependent part of f . This part vanishes in eq. (70).

- Laursen, T. A. (2002). *Computational Contact and Impact Mechanics: Fundamentals of modeling interfacial phenomena in nonlinear finite element analysis*. Springer.
- Padmanabhan, V. and Laursen, T. A. (2001). A framework for development of surface smoothing procedures in large deformation frictional contact analysis. *Finite Elem. Anal. Des.*, **37**:173–198.
- Papadopoulos, P., Jones, R. E., and Solberg, J. M. (1995). A novel finite element formulation for frictionless contact problems. *Int. J. Numer. Meth. Engrg.*, **38**:2603–2617.
- Puso, M. A., Laursen, T. A., and Solberg, J. (2008). A segment-to-segment mortar contact method for quadratic elements and large deformations. *Comput. Methods Appl. Mech. Engrg.*, **197**:555–566.
- Sauer, R. A. (2011). Enriched contact finite elements for stable peeling computations. *Int. J. Numer. Meth. Engrg.*, **87**:593–616.
- Sauer, R. A. and De Lorenzis, L. (2012). A computational contact formulation based on surface potentials. *Comput. Methods Appl. Mech. Engrg.*, (doi:10.1016/j.cma.2012.09.002).
- Simo, J. C. and Armero, F. (1992). Geometrically non-linear enhanced strain mixed methods and the method of incompatible modes. *Int. J. Numer. Meth. Engrg.*, **33**:1413–1449.
- Temizer, I., Wriggers, P., and Hughes, T. J. R. (2011). Contact treatment in isogeometric analysis with NURBS. *Comput. Methods Appl. Mech. Engrg.*, **200**:1100–1112.
- Wriggers, P. (2006). *Computational Contact Mechanics*. Springer, 2nd edition.
- Wriggers, P. (2008). *Nonlinear Finite Element Methods*. Springer.
- Wriggers, P., Krstulovic-Opara, L., and Korelc, J. (2001). Smooth C^1 -interpolations for two-dimensional frictional contact problems. *Int. J. Numer. Meth. Engrg.*, **51**:1469–1495.
- Xu, X.-P. and Needleman, A. (1993). Void nucleation by inclusion debonding in a crystal matrix. *Model. Simul. Mater. Sci. Engrg.*, **1**(2):111–132.
- Yang, B., Laursen, T. A., and Meng, X. (2005). Two dimensional mortar contact methods for large deformation frictional sliding. *Int. J. Numer. Meth. Engrg.*, **62**:1183–1225.